Research Article | Vol. 26, No. 5 | 5 Mar 2018 | OPTICS EXPRESS 6046
Optics EXPRESS

Fabrication and characterization of SiN_x/Au cavities with colloidal nanocrystals

SUZANNE BISSCHOP,[1,2,3] PIETER GEIREGAT,[1,2,3] LUKAS ELSINGER,[2,3] EMILE DRIJVERS,[1,3] DRIES VAN THOURHOUT,[2,3] ZEGER HENS,[1,3] AND EDOUARD BRAINIS[1,3]

[1] *Physics and Chemistry of Nanostructures, Ghent University, Krijgslaan 281-S3, 9000 Ghent, Belgium*
[2] *Photonics Research Group, INTEC Department, Ghent University-IMEC, Sint-Pietersnieuwstraat 41, 9000 Ghent, Belgium*
[3] *Center for Nano and Biophotonics (NB Photonics), Ghent University, B-9000 Ghent, Belgium*
[*] *Zeger.Hens@ugent.be*

Abstract: We demonstrate the fabrication and characterization of on-chip vertically-emitting SiN_x/Au nanopatch cavities containing a monolayer of colloidal quantum dots. The fabrication process is based on electron-beam lithography and deterministically positions both the cavity and the emitters within the cavity with an accuracy of 10 nm. The Purcell enhancement of the spontaneous emission of the quantum dots is studied theoretically and experimentally. The fabrication technique makes it possible to pattern the quantum dot monolayer such that the quantum dots only occupy the center of the nanopatch cavity where a Purcell factor up to 7 can be reached. The work paves the way towards scalable fabrication of bright and directive single-photon sources.

OCIS codes: (220.0220) Optical design and fabrication; (230.3120) Integrated optics devices; (230.6080) Sources.

References and links

1. I. Aharonovich, D. Englund, and M. Toth, "Solid-state single-photon emitters," Nat. Photonics **10**, 631 (2016).
2. N. Somaschi, V. Giesz, L. De Santis, J. C. Loredo, M. P. Almeida, G. Hornecker, S. L. Portalupi, T. Grange, C. Antón, J. Demory, C. Gómez, I. Sagnes, N. D. Lanzillotti-Kimura, A. Lemaítre, A. Auffeves, A. G. White, L. Lanco, and P. Senellart, "Near-optimal single-photon sources in the solid state," Nat. Photonics **10**, 340 EP – (2016).
3. J. Claudon, J. Bleuse, N. S. Malik, M. Bazin, P. Jaffrennou, N. Gregersen, C. Sauvan, P. Lalanne, and J.-M. Gerard, "A highly efficient single-photon source based on a quantum dot in a photonic nanowire," Nat. Photonics **4**, 174–177 (2010).
4. G. Juska, V. Dimastrodonato, L. O. Mereni, A. Gocalinska, and E. Pelucchi, "Towards quantum-dot arrays of entangled photon emitters," Nat. Photonics **7**, 527 EP – (2013).
5. C. Schneider, T. Heindel, A. Huggenberger, P. Weinmann, C. Kistner, M. Kamp, S. Reitzenstein, S. HÃűfling, and A. Forchel, "Single photon emission from a site-controlled quantum dot-micropillar cavity system," Appl. Phys. Lett. **94**, 111111 (2009).
6. M. Arcari, I. Söllner, A. Javadi, S. Lindskov Hansen, S. Mahmoodian, J. Liu, H. Thyrrestrup, E. H. Lee, J. D. Song, S. Stobbe, and P. Lodahl, "Near-unity coupling efficiency of a quantum emitter to a photonic crystal waveguide," Phys. Rev. Lett. **113**, 093603 (2014).
7. G. Kiršanskė, H. Thyrrestrup, R. S. Daveau, C. L. Dreeßen, T. Pregnolato, L. Midolo, P. Tighineanu, A. Javadi, S. Stobbe, R. Schott, A. Ludwig, A. D. Wieck, S. I. Park, J. D. Song, A. V. Kuhlmann, I. Söllner, M. C. Löbl, R. J. Warburton, and P. Lodahl, "Indistinguishable and efficient single photons from a quantum dot in a planar nanobeam waveguide," Phys. Rev. B **96**, 165306 (2017).
8. T. B. Hoang, G. M. Akselrod, and M. H. Mikkelsen, "Ultrafast room-temperature single photon emission from quantum dots coupled to plasmonic nanocavities," Nano Lett. **16**, 270–275 (2016).
9. C. Belacel, B. Habert, F. Bigourdan, F. Marquier, J.-P. Hugonin, S. Michaelis de Vasconcellos, X. Lafosse, L. Coolen, C. Schwob, C. Javaux, B. Dubertret, J.-J. Greffet, P. Senellart, and A. Maitre, "Controlling spontaneous emission with plasmonic optical patch antennas," Nano Lett. **13**, 1516–1521 (2013).
10. M. Cirillo, T. Aubert, R. Gomes, R. Van Deun, P. Emplit, A. Biermann, H. Lange, C. Thomsen, E. Brainis, and Z. Hens, ""flash" synthesis of cdse/cds core–shell quantum dots," Chem. Mater. **26**, 1154–1160 (2014).
11. V. Chandrasekaran, M. D. Tessier, D. Dupont, P. Geiregat, Z. Hens, and E. Brainis, "Nearly blinking-free, high-purity single-photon emission by colloidal inp/znse quantum dots," Nano Lett. **17**, 6104–6109 (2017).
12. K. Lambert, R. K. Čapek, M. I. Bodnarchuk, M. V. Kovalenko, D. Van Thourhout, W. Heiss, and Z. Hens, "Langmuir-schaefer deposition of quantum dot multilayers," Langmuir. **26**, 7732–7736 (2010).

#313739 https://doi.org/10.1364/OE.26.006046
Journal © 2018 Received 23 Nov 2017; revised 9 Feb 2018; accepted 10 Feb 2018; published 28 Feb 2018

Optics EXPRESS

13. W. Xie, R. Gomes, T. Aubert, S. Bisschop, Y. Zhu, Z. Hens, E. Brainis, and D. Van Thourhout, "Nanoscale and single-dot patterning of colloidal quantum dots," Nano Lett. **15**, 7481–7487 (2015).
14. T. B. Hoang, G. M. Akselrod, C. Argyropoulos, J. Huang, D. R. Smith, and M. H. Mikkelsen, "Ultrafast spontaneous emission source using plasmonic nanoantennas," Nat. Commun. **6**, 7788 (2015).
15. P. Kolchin, N. Pholchai, M. H. Mikkelsen, J. Oh, S. Ota, M. S. Islam, X. Yin, and X. Zhang, "High purcell factor due to coupling of a single emitter to a dielectric slot waveguide," Nano Lett. **15**, 464–468 (2014).
16. A. Kinkhabwala, Z. Yu, S. Fan, Y. Avlasevich, K. Müllen, and W. Moerner, "Large single-molecule fluorescence enhancements produced by a bowtie nanoantenna," Nat. Photonics **3**, 654–657 (2009).
17. J. T. Choy, B. J. Hausmann, T. M. Babinec, I. Bulu, M. Khan, P. Maletinsky, A. Yacoby, and M. Lončar, "Enhanced single-photon emission from a diamond-silver aperture," Nat. Photonics **5**, 738–743 (2011).
18. K. Yu, A. Lakhani, and M. C. Wu, "Subwavelength metal-optic semiconductor nanopatch lasers," Opt. Express **18**, 8790–8799 (2010).
19. W. Xie, Y. Zhu, T. Aubert, S. Verstuyft, Z. Hens, and D. Van Thourhout, "Low-loss silicon nitride waveguide hybridly integrated with colloidal quantum dots," Opt. Express **23**, 12152–12160 (2015).
20. W. Xie, Y. Zhu, S. Bisschop, T. Aubert, Z. Hens, D. van Thourhout, and P. Geiregat, "Colloidal quantum dots enabling coherent light sources for integrated silicon-nitride photonics," IEEE J. Sel. Top. Quantum Electron. **23**, 1–13 (2017).
21. C. A. Balanis, *Advanced Engineering Electromagnetics* (Wiley NewYork, 1989).
22. C. Manolatou and F. Rana, "Subwavelength nanopatch cavities for semiconductor plasmon lasers," IEEE J. Quantum Electron. **44**, 435–447 (2008).
23. I. Chung, K. T. Shimizu, and M. G. Bawendi, "Room temperature measurements of the 3d orientation of single cdse quantum dots using polarization microscopy," Proc. Natl. Acad. Sci. **100**, 405–408 (2003).

1. Introduction

The coupling of single-photon emitters to dielectric cavities or plasmonic cavities/antennas has been demonstrated using a variety of physical systems with the aim of making the source brighter and more directive [1]. Some examples include microcavities at cryogenic temperatures [2–5], photonic crystal waveguides [6], nanobeam waveguides [7] and near-field coupling to metallic nano-antennas [8, 9]. Such solid-state single-photon sources are key for optical quantum information processing. Engineering an efficient solid-state single-photon source requires one to address several important challenges, some of which are sometimes overlooked: (i) the single-photon source must be fabricated in a robust, scalable and reproducible manner, (ii) the position of the single-photon source on the chip must be controlled with nanometer to micrometer accuracy (depending on the application), (iii) the fabrication methods must be compatible with a deterministic positioning of a single emitter at the required site within the device with a few nanometer accuracy, (iv) the radiative yield of the single-photon device must be as high as possible and ideally close to one.

With their large absorption cross section and high radiative quantum yield (as high as 90% in the best cases) colloidal core/shell quantum dots (QDs), such as the CdSe/CdS QDs fabricated according to the so-called "flash" synthesis method [10] or the recently demonstrated InP/ZnSe QDs [11], are suitable room-temperature single-photon emitters. Good quality monolayers of such QDs are obtained by Langmuir-Blodgett deposition [12]. We recently showed that such monolayers can be nano-patterned with very high accuracy and demonstrated that single QDs can be isolated at predefined locations with a record success probability of over 40% [13]. However, their deterministic positioning and coupling to resonators still remains challenging. Because of their broad emission line at room-temperature (10-30 nm), the resonator must combine a large resonance linewidth with an ultra-small mode volume. In the past, this has been achieved through plasmonic coupling. Plasmonic coupling has proven to be very effective to speed up radiative decay; e.g. a record 540-fold reduction in the luminescence lifetime has recently been observed in a system consisting of ad hoc positioned QDs and silver nanocubes [8, 14]. The local-field enhancement at the nanocube corners is responsible for this exceptionally strong Purcell effect. In circular cavities and nanostructures, more modest enhancements of the spontaneous emission rates of QDs have been reported before [9, 15], typically of the order of 30 or less. Similar enhancements have also been observed with other types of quantum emitters such as molecules [16] or nitrogen-vacancy centers in diamond nanocrystals [17]. However, devices based

Optics EXPRESS

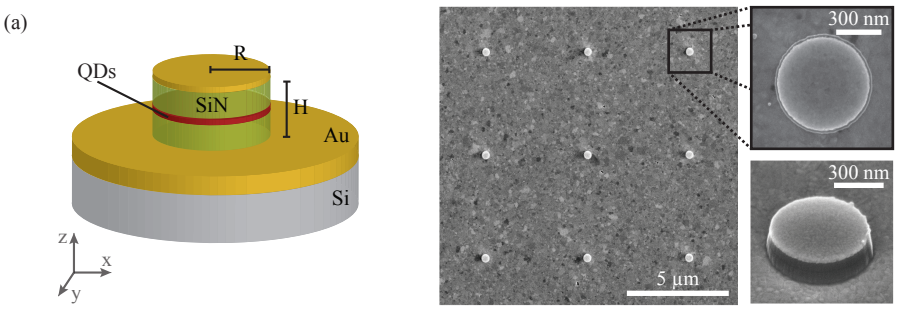

Fig. 1. (a) Schematic representation of a nanopatch cavity with height H and radius R. (b) SEM picture of an array of deterministically positioned nanopatches, and zoom of (top) top view and (bottom) tilted view of a single nanopatch cavity.

on plasmonic coupling usually suffer from non-radiative energy dissipation, significantly reducing their effective quantum yield and precluding their usage for applications where a high radiative quantum yield is of the essence. For instance, in the *nanopatch-cavity* design demonstrated in [9] by Belacel et al., the radiative efficiency was only a few percent.

In this work, we investigate a different circular metallic *nanopatch-cavity* design in which the coupling between the QDs and the scalable circular cavity is dominantly dielectric rather than plasmonic. Our cavities are accurately fabricated using modern and scalable lithographic techniques. They are fully etched to reduce losses and increase the radiative yields of the device up to about 60%, while still providing a broad cavity resonance line and a subwavelength mode volume. This type of resonators has been used in the past to demonstrate small mode volume infrared semiconductor lasing [18]. Also in contrast with [9], in which QDs were transferred to the substrate by dip coating and formed randomly distributed clusters containing a random number of QDs, our cavities contain a uniform monolayer of QDs that can be further patterned down to a single QD, as shown in [13] by Xie et al. In addition, our fabrication method is compatible with any colloidal QD material, such that further optimisation of the SP emitter (eg. through synthesis) can be done independently from the cavity fabrication.

2. Nanopatch cavity structure and fabrication

The nanopatch cavities consist of a monolayer of QDs embedded in a silicon nitride (SiN_x) matrix sandwiched between two gold (Au) layers resulting in subwavelength confinement of the optical resonant modes (see Fig. 1(a)). As the Purcell factor F scales with Q/V, large enhancements are expected for cavities with high Q-factors and small mode volumes. Because the emission line of QDs is broad at room temperature (typically 30 nm), only a low Q-factor of 20 or less is required. From FDTD simulations (see section 3), Purcell factors of 5-10 are nevertheless expected for a single QD in the center of the cavity, due to the small mode volume. A fabrication process was designed that allows for the fabrication of large arrays of such cavities with fixed height H and varying radii R. Figure 1(b) shows a small area of such an array in which cavities with a radius of 300 nm were formed every 5 µm. Figure 2(a) schematically shows the fabrication flow of the nanopatches. First, 2-3 nm of titanium (adhesion layer) is sputtered onto a silicon wafer, followed by the evaporation of a 100 nm thick Au layer. Note that such a Ti layer is deposited before each of the following Au deposition steps. Next a 60 nm SiN_x layer is deposited using an optimized plasma-enhanced chemical vapor deposition (PECVD) process at a temperature of 120 °C [19]. A low plasma frequency is chosen to reduce the optical loss as well as the material luminescence of the SiN_x layer. Next cross-shaped Au markers are patterned using electron-beam

Optics EXPRESS

(e-beam) lithography and a standard lift-off process. These markers are used in the following lithographic steps to ensure that the QDs are accurately positioned at the center of the cavity. The deposition of the QDs follows the process developed in [13] and constitutes the next three steps depicted in Fig. 2(a). It consists of (ii) the definition of the deposition area by e-beam lithography, (iii) the formation of a uniform QD-monolayer using Langmuir-Blodgett deposition, and (iv) a lift-off step to remove the QDs covering the e-beam resist. We used oleate-passivated CdSe/CdS core/shell QDs synthesized by a seeded-growth "flash" approach [10] with a core diameter of 3.1 nm, total diameter of 9.5 nm and a central emission peak of 630 nm. After the patterning step, circular patches of monolayer-QDs stay behind. Their quality was examined using a high-resolution scanning electron microscope (SEM) (FEI Nova 600), see Fig. 2(b). By automated image recognition, the QD-patches were accurately aligned with respect to the Au-markers, allowing to deterministically position them in the center of the cavities and leave no QD outside the cavities. This technique provides a good control of both the quality and thickness of the QD layer, which is important to control the shape of the pattern and the *number of QDs* per cavity which can be controlled down to a single QD with a high probability of success, as demonstrated in [13].

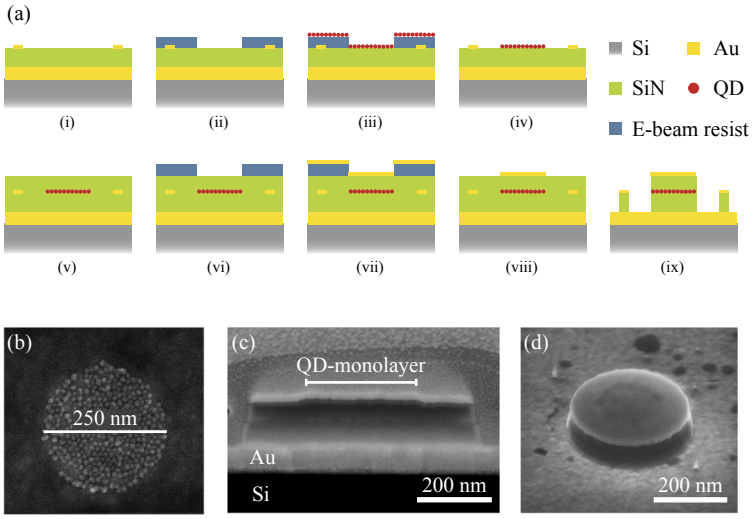

Fig. 2. (a) Schematic representation of the different fabrication steps, (b) Disk-shape patterned monolayer of QDs, (c)-(d) Illustration of alignment accuracy: cross-section of a cavity of radius R = 300 nm with a QD monolayer forming a circular patch of radius 150 nm right in the center of the cavity. Tilted view of the same cavity shown in (c). The height difference caused by the QD-pattern can be seen in the top Au layer.

A second 60 nm SiN_x layer is subsequently deposited using the same PECVD process for embedding the QDs, as shown in step (v). As demonstrated in previous work [20], this low temperature SiN_x deposition is crucial for preserving the luminescent properties of the QDs, such as a high quantum yield. The size and shape of the circular top Au layer (40 nm thickness), which define the resonant wavelength, are precisely controlled during a final e-beam lithography step (vi) and lift-off step (vii)-(viii). The deposition of the Au patches is again aligned with respect to the Au markers. Finally, the resonators are etched using an optimized dry etching process (RIE with CF4/H2), in which the top Au disks act as a hard mask. As a demonstration of our alignment accuracy, we fabricated patches in which the QD patches have a diameter two times smaller than the cavity itself. The result is displayed in Figs. 2(c) and 2(d), where a cross-section and a tilted view of the final cavity are shown. In both SEM-pictures the area containing the QDs is clearly

Optics EXPRESS

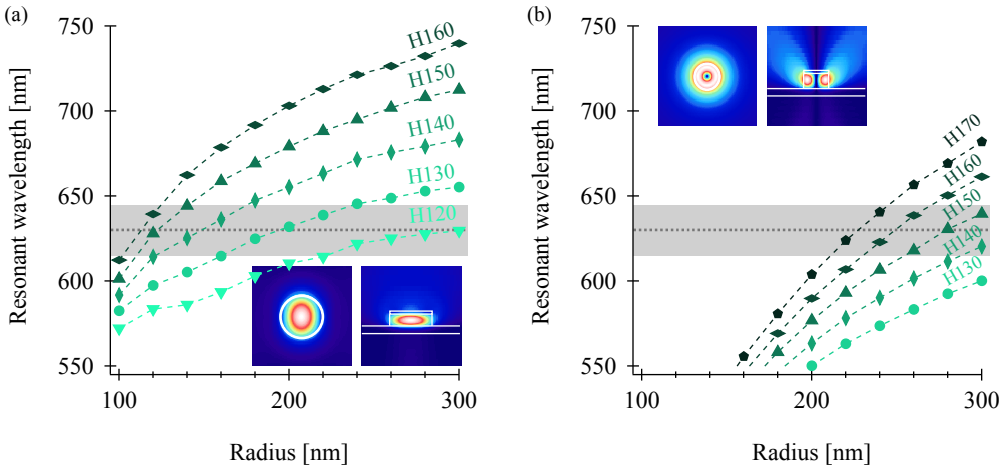

Fig. 3. Resonant wavelength of the (a) TM_{111} and (b) TE_{011} modes as a function of cavity dimensions radius R and height H (ranging from 120 nm to 170 nm, see data labels). The central emission wavelength and linewidth of the QDs, which were integrated in the cavities, are indicated in grey. The insets show the top and side view of the magnitude of the electric field mode profiles.

visible and it can be seen that they are patterned exactly in the center. The process-flow allows us to deterministically position the QDs in the cavity, and align the cavity itself on the chip with an accuracy of 10 nm, which corresponds to roughly the size of one QD.

3. Optical modes in the nanopatch cavity

Depending on the dimensions of the cavities, various optical modes are supported. We are interested in the subwavelength modes that exhibit small optical loss and a large spatial and spectral overlap with our active material. We present FDTD simulation results for the fundamental quasi-TM_{111} and quasi-TE_{011} modes; the analytical expressions of these modes have been reported in literature [21, 22]. In all our simulations, the thickness of the top and bottom Au layers was taken to be 40 nm and 100 nm, respectively.

In order to characterize these modes, we first determined their resonance wavelength λ_{res} as function of cavity parameters H and R. The results for TM_{111} and TE_{011} modes are shown in Figs. 3(a) and 3(b) respectively. The TE mode does not couple well with the surface plasmons and requires a larger cavity dimension to achieve the same mode wavelength compared to the TM mode. The central wavelength of a TE mode is also more sensitive to the radius of the cavity. The horizontal dotted line represents the emission wavelength of our QDs (630 nm) and the grey area around it corresponds to the FWHM of the QDs emission line. By selecting the cavity height and the cavity radius such that λ_{res} falls in the center of the grey region, a resonance with the QD emission is achieved. The spatial energy distributions of these modes (top and side views) are also shown as insets in Fig. 3. The FDTD simulations also provides the FWHM of the cavity lines ($\Delta\lambda$), from which the quality factor $Q = \lambda_{res}/\Delta\lambda$ can be deduced. Q-factors were only computed for those cavities that support a mode resonating with the QDs. We found Q-factors in the 10-15 range for the TM-modes and in the 13-16 range for the TE-modes.

Next we calculated the radiative decay rates Γ_i ($i \in \{x, y, z\}$) of classical dipoles oscillating in the x, y and z directions. In a structured environment, the decay rates Γ_i usually differ from each other and lead to an enhancement (or inhibition) characterized by the Purcell factor $F_i = \Gamma_i/\Gamma_{hom}$, where Γ_{hom} is the decay rate the dipole would have in a homogeneous medium. The highest

Optics EXPRESS

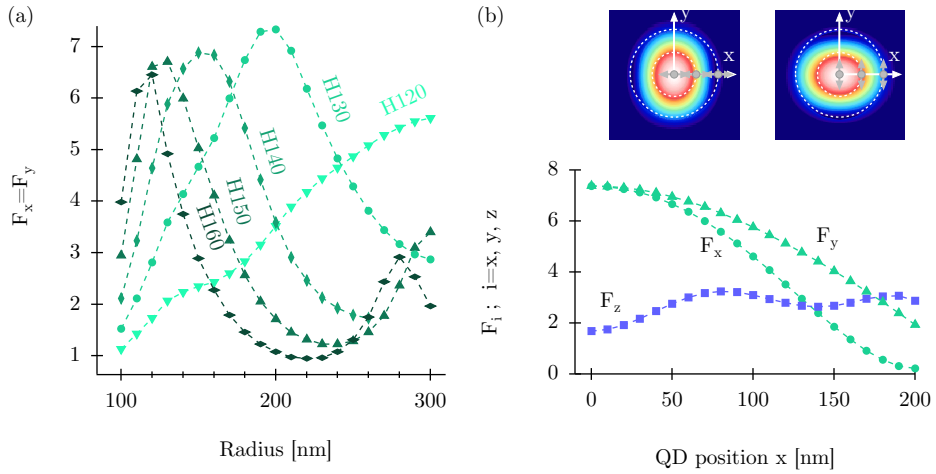

Fig. 4. (a) Purcell factor $F_x = F_y$ for a linear dipole (emitting at 630 nm) positioned at the center of the cavity as a function of cavity radius R for five different cavity heights H ranging from 120 to 160 nm. The maxima of each curve corresponds to resonance with TM_{111} modes. (b) Purcell factors F_i ($i \in \{x, y, z\}$) as a function of dipole position x in a cavity with $H = 130$ nm and $R = 200$ nm. The insets show the mode profiles of the two hybrid TM_{111} modes excited by an $x-$ and $y-$ polarised dipole respectively.

enhancement is found when the dipole is placed at the position of the highest mode field intensity and has a polarization tangential to the electric field lines. In the case of a linear dipole coupled to a TM_{111} mode, this occurs for an electric dipole positioned in the center of the cavity with the dipole moment in the xy-plane. The dipole then couples to the TM_{111} mode with field lines parallel to the polarization direction of the linear dipole [18]. Figure 4(a) shows the values of the Purcell factor F_x at wavelength 630 nm for a x-polarized dipole at the center of the cavity with varying cavity dimensions (for symmetry reasons, the result is the same for a y-polarized dipole, thus $F_y = F_x$). It can be seen that the highest enhancement ($F_x = F_y = 7.4$) is found for a cavity with height $H = 130$ nm and radius $R = 200$ nm. The same analysis for the TE_{011} mode (which has field lines circulating around the center of the cavity [18]) shows that the highest Purcell factor is obtained for an electric linear dipole positioned at a distance $0.75\ R$ from the cavity center with its dipole moment in the cavity plane in the direction orthogonal to that displacement. By sweeping through the values of H and R, the highest Purcell factor found in this case is slightly smaller than 4. Because the TM_{111} mode offers a larger Purcell enhancement, we decided to design our nanopatch cavities for the TM_{111} modes.

Consider a cavity geometry supporting a resonant TM_{111} mode at 630 nm, e.g. $R = 200$ nm and $H = 130$ nm. When the linear dipole is moved away from the cavity center, the coupling to the TM_{111} modes changes, and so does the enhancement of the spontaneous decay rate. Figure 4(b) shows the evolution of the Purcell factors F_x, F_y and F_z when the dipole is displaced in the x-direction. The factors F_x and F_y do not evolve exactly in the same manner because dipoles vibrating in the x- and y-directions couple to hybrid TM_{111} modes with different intensity profiles which are slightly elongated in the direction orthogonal to the E-field in the center of the cavity. Note that a dipole vibrating in the z-direction does not experience much Purcell enhancement. This is in striking contrast with the nanopatch cavities of Belacel et al. [9], in which F_z factors of the order of 50 have been reached by plasmonic coupling at the expense of very large optical losses.

Optics EXPRESS

4. Effect of random QD orientation and position

Low temperature measurements reveal that QD excitons can recombine though π (linear dipole along the QD c-axis) and $\sigma_\pm$ (circular dipoles in the plane orthogonal to the QD c-axis) transitions within the fine structure of the fundamental excitonic line [23]. At room temperature, the relative strengths of these transitions (f_π, f_{σ_+}, and f_{σ_-}) depend on the size and geometry of the QD. The average Purcell factor experienced by a QD can be written as

$$F = \sum_{\chi\in\{\pi,\sigma_+,\sigma_-\}} f_\chi \, F_\chi(r,\vec{\Omega}), \tag{1}$$

where r stands for the distance of the QD to the cavity center and $\vec{\Omega} = (\theta,\varphi)$ for the orientation of the QD c-axis with respect to the z-axis of the cavity. The analysis can be greatly simplified if one neglects the mode profile difference between the x- and y-polarized TM_{111} modes (see Fig. 4(b)), i.e. one assumes that $F_x \approx F_y$ and that a linear dipole vibrating in the xy-plane experiences a Purcell enhancement $F_\parallel = (F_x + F_y)/2$ while a linear dipole vibrating in the z-axis direction experiences a Purcell enhancement $F_\perp = F_z$. With this simplification, F_χ does *not* depend on the azimuthal angle φ and

$$F_\pi(r,\theta) = F_\parallel(r)\sin^2\theta + F_\perp(r)\cos^2\theta \tag{2a}$$

$$F_{\sigma_\pm}(r,\theta) = \frac{1}{2}\left[F_\parallel(r)(1+\cos^2\theta) + F_\perp(r)\sin^2\theta\right]. \tag{2b}$$

Because of the spatial dependence of $F_\parallel(r)$ and $F_\perp(r)$ and random orientation of the c-axis of the QDs, the spontaneous decay from a monolayer of QDs is expected to be highly multi-exponential.

Consider the emission from a QD at a distance r from the cavity center. In order to take into account the random direction of its c-axis, any emission-related property would have to be averaged. Assuming a uniform statistical distribution of c-axis directions, the orientation average reads:

$$\langle\ldots\rangle_\theta = \int_0^{\frac{\pi}{2}} \ldots \sin\theta \, \mathrm{d}\theta = \int_{F_{\min}}^{F_{\max}} \ldots \; P_\chi(F;r) \; \mathrm{d}F, \tag{3}$$

where $P_\chi(F;r)$ is the statistical distribution of the Purcell factor resulting from the random distribution of the polar angle θ, $F_{\min} = \min\left[F_\parallel(r), F_\perp(r)\right]$, and $F_{\max} = \max\left[F_\parallel(r), 1/2\left(F_\parallel(r) + F_\perp(r)\right)\right]$. The distribution $P_\chi(F;r)$ can be deduced from the functional relationship between F and θ in Eqs. (2). It depends on whether the emission is a π or σ transition:

$$P_\pi(F;r) = \frac{1}{2}\left[\left(F_\parallel(r) - F_\perp(r)\right)\left(F_\parallel(r) - F\right)\right]^{-\frac{1}{2}} \tag{4a}$$

$$P_{\sigma_\pm}(F;r) = \left[\left(F_\parallel(r) - F_\perp(r)\right)\left(F_\parallel(r) + F_\perp(r) - 2F\right)\right]^{-\frac{1}{2}}. \tag{4b}$$

Figure 5(a) compares the distributions $P_\pi(F;r)$ and $P_{\sigma_\pm}(F;r)$ for a QD located in the center of a nanopatch cavity of height $H = 130$ nm and radius $R = 200$ nm and for a QD located 180 nm away from the center. The understanding of the emission from a circular QDs monolayer of radius $R_{\mathrm{ml}} \leq R$ (see Figs. 2(b)–2(d)) requires an additional spatial-averaging step

$$\langle\ldots\rangle_r = \frac{2}{R_{\mathrm{ml}}^2}\int_0^{R_{\mathrm{ml}}} \ldots \; r \, \mathrm{d}r. \tag{5}$$

Figure 5(b) shows the space-averaged Purcell factor distributions $P_\pi(F) = \langle P_\pi(F;r)\rangle_r$ and $P_{\sigma_\pm}(F) = \left\langle P_{\sigma_\pm}(F;r)\right\rangle_r$ for a monolayer of QDs filling a nanopatch cavity of height $H = 130$ nm and radius $R = 200$ nm ($R_{\mathrm{ml}} = R$). Despite qualitative differences, both distributions span a broad range of Purcell factors ranging from 1 to 7.4, have the same average value $\bar{F} = \bar{F}_\pi = \bar{F}_{\sigma_\pm} = 3.4$, and are expected to result in very similar non-exponential decay traces.

Optics EXPRESS

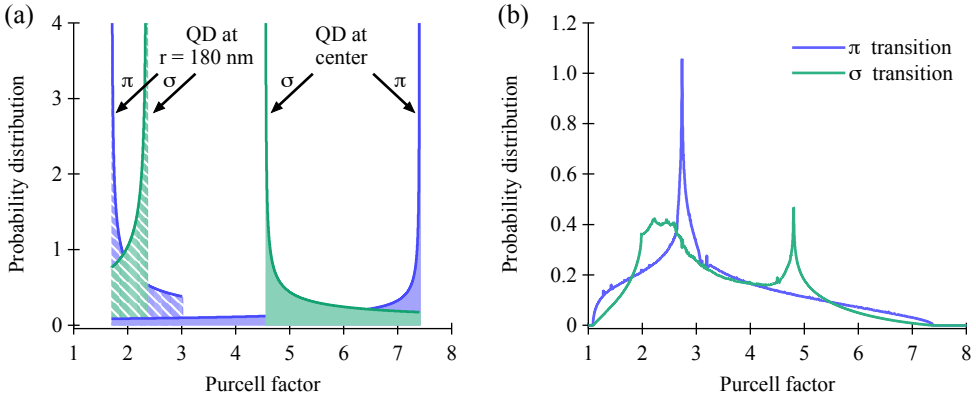

Fig. 5. (a) Statistical distributions of the Purcell factor $P_\pi(F;r)$ and $P_{\sigma_\pm}(F;r)$ for a QD in the center of a nanopatch cavity of height H = 130 nm and radius R = 200 nm, and 180 nm away from the center. (b) Statistical distributions of the Purcell factor $P_\pi(F)$ and $P_{\sigma_\pm}(F)$ in a monolayer of QDs filling the same nanopatch cavity.

5. Measurements and results

Our CdSe/CdS core/shell QDs have a peak emission at 630 nm and a luminescence quantum yield of 60-75%. When dispersed in toluene (refractive index n = 1.5), the decay is almost single-exponential, see the black dots in Fig. 6(a), with an average decay time $\bar{\tau}_{\rm tol}$ = 40.7 ns. We define the average decay time of a decay trace $I(t)$ as

$$\bar{\tau} = \frac{\int_0^\infty t\, I(t)\, {\rm d}t}{\int_0^\infty I(t)\, {\rm d}t}. \tag{6}$$

A bi-exponential fit (red trace in Fig. 6(a)) shows one principal (short) decay time $\tau_{{\rm tol},1}$ = 33.0 ns accounting for 4/5 of the decay and one secondary (long) decay time $\tau_{{\rm tol},2}$ = 72.3 ns accounting for 1/5 of the decay.

In a first experiment, we fabricated a reference sample with a monolayer of QDs embedded between two 60 nm layers of SiN_x. Since SiN_x has a higher index of refraction than toluene (n = 1.86), additional dielectric screening was expected to shorten the radiative decay time. Indeed, the radiative decay time $\tau(n)$ of a QD embedded in an homogeneous medium of index n is connected to the radiative decay time τ_0 of the QD in vacuum through the relation $\tau(n) = \tau_0/(n\,|f_{\rm LF}|^2)$, where

$$f_{\rm LF}(n) = \frac{3\,n^2}{\varepsilon + 2\,n^2} \tag{7}$$

is the *local field factor* and ε the complex relative permittivity of the QD (ε = 7.05+i 0.06 at 630 nm for our CdSe/CdS QDs). For this reason, a lifetime shortening by a factor $\tau(1.86)/\tau(1.5)$ = 0.5 was expected, leading to bi-exponential decay, as in toluene, but with lifetimes $\tau_{{\rm SiN_x},1}$ = 16.5 ns and $\tau_{{\rm SiN_x},2}$ = 36.1 ns. This theoretical prediction is displayed by the dashed red line in Fig. 6(a). The experimental decay trace from our sample is also shown in Fig. 6(a) (blue dots) for comparison. The agreement with the local field theory is very good, though not perfect. A bi-exponential fit (yellow plain trace in Fig. 6(a)) of the experimental data shows that the fast decay time is a bit smaller than expected ($\tau_{{\rm SiN_x},1}$ = 13.3 ns) while the slow decay time is almost identical ($\tau_{{\rm SiN_x},2}$ = 39.5 ns). This demonstrates that the Langmuir-Blodgett deposition of the QDs and their embedding in SiN_x does not significantly degrade the emission quantum yield. The average decay time of QDs embedded in SiN_x is $\bar{\tau}_{\rm SiN}$ = 22.9 ns.

Optics EXPRESS

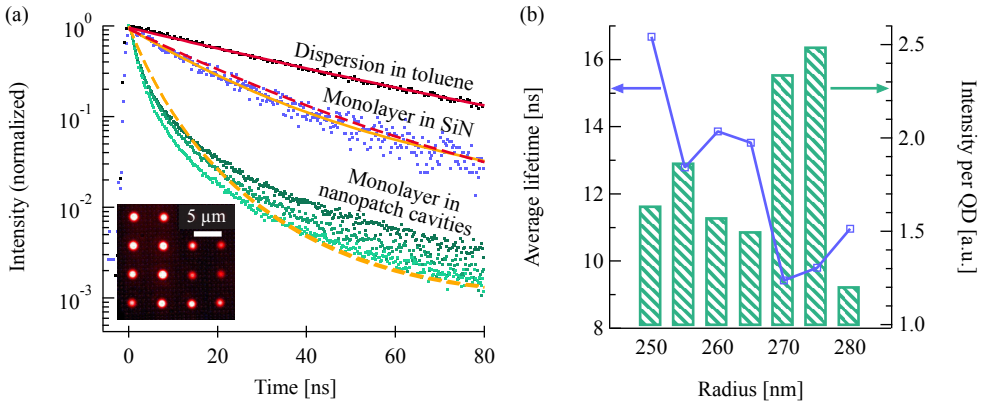

Fig. 6. (a) PL decay traces from QDs embedded in nanopatch cavities of height H = 130 nm and radii R = 260, 270, and 280 nm (green dots) show Purcell reduction of the luminescence decay time compared to: the same QDs suspended in toluene (black dots) and a monolayer of QDs embedded between two 60 nm thick layers of SiN_x (blue dots). The plain lines (red and yellow) are bi-exponential fits to the data. The dashed lines (red and yellow) are theoretical predictions (explanations in the text). Inset: PL image from an array of nanopatch cavities with height H = 130 nm under cw excitation at 445 nm. (b) Average PL decay times (blue squares) and PL intensity per QD (histogram) in nanopatch cavities as a function of the cavity radius R.

The luminescence decay from the nanopatch cavities was investigated using a micro-photoluminescence setup. The excitation beam at 445 nm was produced by a PicoQuant LDH-D-C-440M laser diode. The laser diode operates in either cw or pulsed mode (in which case it produces short pulses of less than 100 ps at a variable repetition rate in the kHz-MHz range). The excitation beam was focused on the sample using a 100× Olympus objective lens and shaped using a digital micro-mirror device (Texas Instrument, 0.55" XGA 2x LVDS DMD) to allow custom excitation patterns (e.g. exciting a single micrometer-sized spot or the entire field of view). The luminescence was collected through the same objective lens and directed either to an imaging spectrometer (Andor Shamrock 330i) equipped with an EMCCD camera (Andor iXon DU897) or to a photon-timing setup consisting of a silicon photon-counting module (Perkin Elmer SPCM-AQRH-14) with a time resolution of about 500 ps and start-stop time correlator (PicoQuant, PicoHarp 300).

The inset of Fig. 6(a) shows the photoluminescence (PL) image of an array of nanopatch cavities under cw excitation as captured by the EMCCD camera. The sample consists of an array of cavities with the same height H = 130 nm, but different radii. When excited with short pulses at 445 nm, the PL of the QDs embedded in the nanopatch cavities produces highly non-exponential decay traces $I(t)$. The fastest decays were observed in cavities with radii R = 260, 270, and 280 nm; these are represented in Fig. 6(a) by green dots of different tones. For every cavity tested, the average decay time $\bar{\tau}$ ranged between 9.4 ns and 16.7 ns, see the blue data points in Fig. 6(b). The cavity showing the strongest lifetime shortening ($\bar{\tau}$ = 9.4 ns) had a radius R = 270 nm (light-green decay trace in Fig. 6(a)). According to simulations, the cavity radius realizing the resonance condition was R = 200 nm. The discrepancy between the theory and experiment is due to the fact that the cavity height is difficult to control with an accuracy of 10 nm during the fabrication process and also difficult to estimate with that accuracy from the cavity cross-sections (see Fig. 2(c)). According to Fig. 3(a), the resonance condition for a cavity of radius R = 270 nm is fulfilled if the height is H = 123 nm. For that cavity height, the maximum Purcell enhancement

Optics EXPRESS

$F_{\parallel}$ in the center of the cavity would be slightly reduced (~ 6 instead of 7.4).

In order to compare the experimental decay traces to the theoretical one expected for the optimal cavity design (H = 130 nm, R = 200 nm), we also plotted the decay

$$I_{\chi}(t) = \int I_{\mathrm{SiN_x}}\left(t; \frac{\tau_{\mathrm{SiN_x},1}}{F}, \frac{\tau_{\mathrm{SiN_x},2}}{F}\right) P_{\chi}(F)\, \mathrm{d}F + B \tag{8}$$

in Fig. 6(a) (dashed orange line), where $I_{\mathrm{SiN_x}}\left(t; \tau_{\mathrm{SiN_x},1}, \tau_{\mathrm{SiN_x},2}\right)$ is the bi-exponential fit to the decay data in SiN_x, $P_{\chi}(F)$ ($\chi \in \{\pi, \sigma_{\pm}\}$) are the Purcell factor distributions displayed in Fig. 5(b), and $B = 10^{-3}$ a constant mimicking the experimental background noise. Remarkably, $I_{\pi}(t) \approx I_{\sigma_{\pm}}(t)$: the difference between the two functions is barely noticeable, resulting in a single characteristic non-exponential decay. According to simulations, ~ 60% of the total energy radiated by a dipole located in the center of the cavity, where the coupling to the mainly vertical emitting TM mode is best, is radiative while the rest is dissipated. When pumped at 445 nm, the luminescence I of a nanopatch cavity is expected to be proportional to the number of emitters N_{QD} in the cavity and inversely proportional to the emitter decay time. In Fig. 6(b), we plotted the luminescence intensity per QD I/N_{QD} (histogram) as a function of the cavity radius. As expected, cavities with shorter decay times tend to emit more photons per QD. The product $I/N_{QD} \times \bar{\tau}$ is equal to 23.24 in average with a standard deviation of 1.9. However, some cavities showed less luminescence than expected, likely because of structural defects causing a less favorable balance between radiation and dissipation.

6. Conclusion

We have developed a straightforward fabrication method, based on e-beam lithography that allows a precise control on the positioning of emitter and cavity. More specifically we demonstrated that a uniform monolayer of colloidal QDs can be precisely positioned in the center of a sub-wavelength SiN_x/Au cavity, which can be further patterned down to a single QD in future experiments. However to develop such a single photon source, it is crucial to study the SP properties of the emitter itself, to determine which kind of dots have superior SP properties (eg. InP/ZnSe as shown in [11]) and more importantly, which ones preserve these properties after embedding/patterning them. As our fabrication method is compatible with any colloidal QD material, the final combination of the best emitter with our nanoptach cavities does not pose any additional challenges. Finally we have also studied and clarified the non-exponential behaviour of the decay traces when an emitter is placed off center or in the case of a film of multiple emitters. Although the speed-up of the spontaneous emission of these QD monolayers is modest, the expected radiative efficiency for these single photon cavities is high compared to plasmonic cavities with stronger Purcell enhancement. The circular shape of our cavities, together with the mode profile of the targeted mode and the possibility to deterministically position both cavity and emitter allows for a robust and reproducible source. As the patterning and cavity fabrication can be seen as two independent fabrication steps with respective yields of 40% and 100%, we can estimate that the yield of these scalable single photon sources can be up to 40%.

Funding

Belgian Science Policy Office (IAP 7.35, photonics@be); H2020 Marie Sklodowska-Curie actions (Phonsi H2020-MSCA-ITN-642656); FWO-Vlaanderen (FWO17/PRJ/380); Ghent University (GOA 01G01513); IWT-Vlaanderen; H2020 European Research Council (ERC).